# Interconnected Carbon Nanosheets Derived from Hemp for Ultrafast Supercapacitors with High Energy

Huanlei Wang,[†,‡] Zhanwei Xu,[†,‡] Alireza Kohandehghan,[†,‡] Zhi Li,[†,‡,*] Kai Cui,[‡] Xuehai Tan,[†,‡] Tyler James Stephenson,[†,‡] Cecil K. King'ondu,[†,‡] Chris M. B. Holt,[†,‡] Brian C. Olsen,[†,‡] Jin Kwon Tak,[§] Don Harfield,[§] Anthony O. Anyia,[§] and David Mitlin[†,‡,*]

[†]Chemical and Materials Engineering, University of Alberta, Edmonton, Alberta T6G 2 V4, Canada, [‡]National Institute for Nanotechnology (NINT), National Research Council of Canada, Edmonton, Alberta T6G 2M9, Canada, and [§]Bioresource Technologies, Alberta Innovates-Technology Futures, Vegreville, Alberta, T9C 1T4, Canada

ABSTRACT We created unique interconnected partially graphitic carbon nanosheets (10—30 nm in thickness) with high specific surface area (up to 2287 $m^2 g^{-1}$), significant volume fraction of mesoporosity (up to 58%), and good electrical conductivity (211—226 S m^{-1}) from hemp bast fiber. The nanosheets are ideally suited for low (down to 0 °C) through high (100 °C) temperature ionic-liquid-based supercapacitor applications: At 0 °C and a current density of 10 A g^{-1}, the electrode maintains a remarkable capacitance of 106 F g^{-1}. At 20, 60, and 100 °C and an extreme current density of 100 A g^{-1}, there is excellent capacitance retention (72—92%) with the specific capacitances being 113, 144, and 142 F g^{-1}, respectively. These characteristics favorably place the materials on a Ragone chart providing among the best power—energy characteristics (on an active mass normalized basis) ever reported for an electrochemical capacitor: At a very high power density of 20 kW kg^{-1} and 20, 60, and 100 °C, the energy densities are 19, 34, and 40 Wh kg^{-1}, respectively. Moreover the assembled supercapacitor device yields a maximum energy density of 12 Wh kg^{-1}, which is higher than that of commercially available supercapacitors. By taking advantage of the complex multilayered structure of a hemp bast fiber precursor, such exquisite carbons were able to be achieved by simple hydrothermal carbonization combined with activation. This novel precursor-synthesis route presents a great potential for facile large-scale production of high-performance carbons for a variety of diverse applications including energy storage.
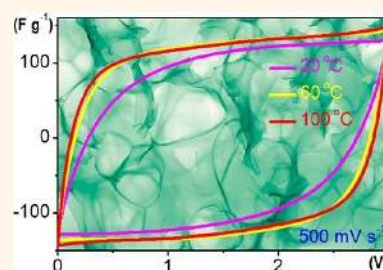
KEYWORDS: biomass · carbon nanosheets · ionic liquid · supercapacitor · energy storage

Electrochemical capacitors (known as ultracapacitors or supercapacitors) based on electrical double layer (EDL) charge accumulation hold promise for a wide range of applications, including portable electronics, uninterruptable power sources, medical devices, load leveling, and hybrid electric vehicles.[1,2] Conventional organic electrolytes used in EDL supercapacitors contain a mixture of a solvent and a salt. However, the exclusive use of organic electrolytes may limit the broadening of the supercapacitors' commercial application base, since solvents such as acetonitrile have issues associated with their flammability at elevated temperatures, as well as their toxicity and environmental impact. Alternative electrolytes based on solvent-free ionic liquids possess several advantages over organic ones, including higher operating voltage windows (>3 V *vs* ~2 V), lower toxicity, negligible vapor pressure, and much better

thermal stability.[3] Unfortunately, supercapacitors based on ionic liquids normally perform well only at temperatures near or above 60 °C.[4,5] The room temperature performance, which is an essential prerequisite for most commercial applications, remains poor due to ionic liquid's high viscosity and low ionic diffusivity. Moreover, large cation and anion sizes limit the usefulness of conventional microporous activated carbon electrodes since the ions either literally do not fit into pores or become diffusion limited at required scan rates.[6,7] It is only with custom tailored eutectic ionic liquids that lower temperature performance may be achieved using carbon nanotubes and carbon onions.[3]

Activated carbons,[8] templated carbons,[9] carbon nanofibers,[10] carbon nanotubes,[11] carbide-derived carbons,[12] and graphene[13,14] have been intensively investigated for supercapacitor electrode applications. Among

them, activated carbons have been successfully developed as electrodes for commercial supercapacitor devices.[15] Commercial high surface area "electrode-grade" activated carbons usually possess moderate gravimetric capacitances in the range of $100-120$ F g^{-1} in an organic electrolyte.[2,6] Depending on the commercial source, activated carbons are derived from pyrolysis of agricultural wastes or from the coking operation during petroleum refining.[16] Recently, outstanding specific capacitances of $200-300$ F g^{-1} in organic electrolyte or ionic liquid have been reported by employing improved activated carbon electrodes, with tailored pore size distributions.[17,18] However the power characteristics of many of these carbons remain limited due to an intrinsically high fraction of microporosity, which in turn limits pore accessibility of the electrolyte ions at high scan rates.[6]

It is becoming well understood that the key to achieving high power in porous electrodes is to reduce the ion transport time. The ion transport time (τ) can be expressed by the equation $\tau = l^2/d$, where l is the ion transport length and d is the ion transport coefficient.[19] From that vantage, carbons with open 2D type morphology possess an intrinsic advantage over particulate type systems since the ion transport length is significantly shortened in the thin dimension.[20] Therefore nanomaterials based on graphene and their hybrids have emerged as a new class of promising high-rate electrode candidates.[13,21] Activated graphene, curved graphene, laser-scribed graphene, ultrathin planar graphene, and sponge-like graphene,[15,22−25] which possess large open and relatively flat adsorption surfaces in addition to high in-plane electrical conductivity, have excellent electrochemical performance with energy—power combinations often much superior to that of activated carbons. Widely used methods for synthesis of graphene-like materials include a modified Hummers method, chemical vapor deposition, and microwave synthesis.[22,25,26] Unfortunately even the most economically produced graphene-like material is nowhere near cost competitive with petroleum- or biowaste-derived carbons achieved *via* simple pyrolysis or hydrothermal methods.[16] Biomass, which mainly contains cellulose, hemicelluloses, and lignin biopolymers, is widely utilized as a feedstock for activated carbon production.[17,27,28] What would be ideal is to employ a relatively green carbonization method to create nanosheets with graphene-like morphology, rather than activated carbon-like particulates, using such precursors.

Hemp (*Cannabis Sativa L.*) has been cultivated for centuries since it grows quickly without any special requirements for climate, pesticides, or fertilizer. Besides the ancient applications for rod, sails, and clothing, hemp is currently being used for paper, building materials, food, medicine, oil, fuel, and in the plastics industry. Conventionally carbonized hemp fiber has also been recently prepared, with activation being achieved *via* water, $ZnCl_2$, and H_3PO_4.[29−31] Though the products were not fully tested for electrochemical energy storage it is expected that they would perform entirely analogously to other forms of pyrolyzed carbon particulates. Here, we report a combined hydrothermal and activation processes that uses hemp bast fiber as the precursor to achieve graphene-like carbon nanosheets. The interconnected two-dimensional carbon nanosheets also contain very high levels of mesoporosity. Such structures are quite unique, and as expected they display remarkable electrochemical properties in a conventional ionic liquid electrolyte.

RESULTS AND DISCUSSION

Supplementary Figure S1 presents photographs of the hemp bast fiber before and after hydrothermal carbonization. The hydrothermal process caused the material, which initially resembled a macroscopic yarn, to break up into smaller pieces. The subsequent activation with KOH generated the carbon nanosheets, denoted by CNS-*X*, where *X* refers to the activation temperature (in °C). Figure 1a shows a scanning electron microscopy (SEM) micrograph, highlighting the highly interconnected sheet-like structure of sample CNS-800. Supplementary Figure S2 shows the SEM micrographs of CNS-700 and CNS-750, demonstrating a similar structure in the lower activation temperature specimens. The macroporous voids, as shown in the SEM images, are beneficial since during electrochemical testing they can serve as ion-buffering reservoirs.[32]

Figure 1b shows a transmission electron microscopy (TEM) micrograph that further highlights the structure of CNS-800, which consists of highly interconnected carbon nanosheets. Figure 1c shows a high resolution TEM micrograph that highlights the porous partially ordered structure of CNS-800. Additional images of CNS-800 are shown in Supplementary Figure S3. Figure 1d and Supplementary Figure S4 show annual dark field (ADF) TEM micrographs and electron energy loss spectroscopy (EELS) thickness profiles (inset) of CNS samples. The CNS specimens had a generally similar structure, though with slightly differing thicknesses. The thickness of the individual carbon nanosheets decreased with the increase of activation temperature, which is in the range of $50-100$ nm for CNS-700, $40-70$ nm for CNS-750, and $10-30$ nm for CNS-800.

Combining the unique structure of the hemp bast fiber with a hydrothermal synthesis treatment is critical to achieve the carbon nanosheet morphology. Hemp bast fiber has a multilevel layered structure composed of cellulose, semicellulose, and lignin.[33−35] As schematically illustrated in Scheme 1, the wall of a hollow hemp fiber ($10-30$ μm in diameter) is mainly composed of three layers. The internal (S3) and outer (S1) layers are mainly composed of semicellulose and lignin while the middle layer (S2) is primarily crystalline cellulose ($\sim$70 wt %). The S2 layer, which makes up
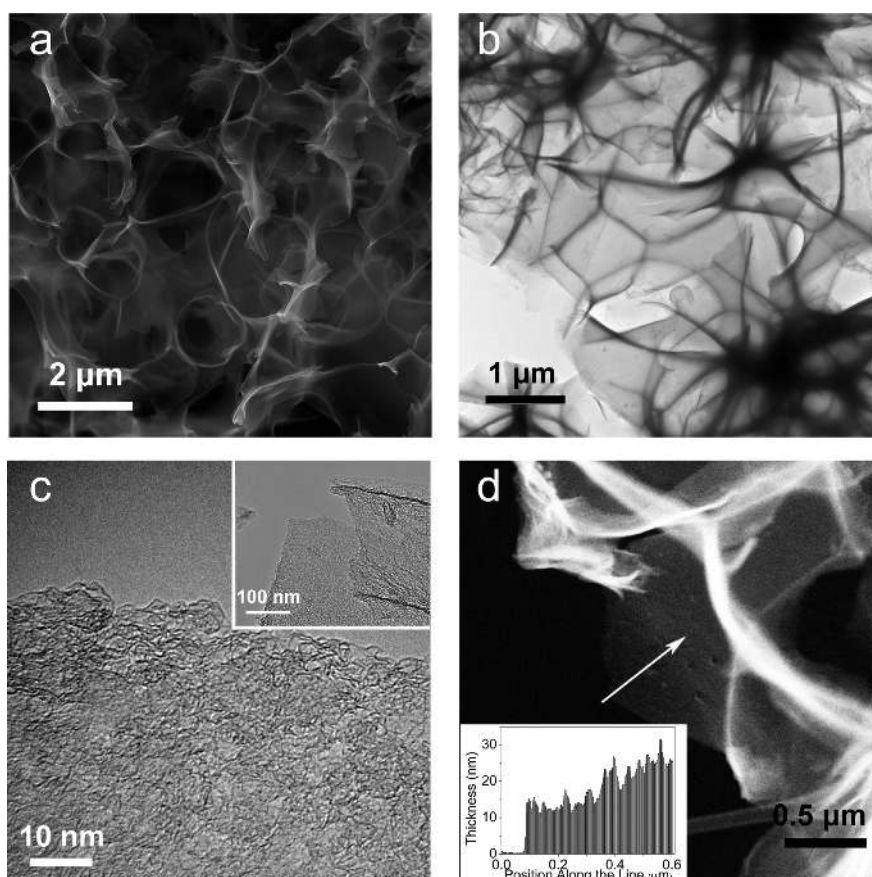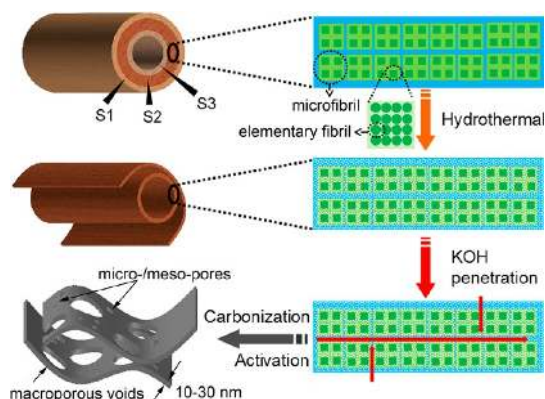
Figure 1. (a) SEM micrograph highlighting the interconnected 2D structure of sample CNS-800. (b) TEM micrograph highlighting the structure of CNS-800. (c) High resolution TEM micrograph highlighting the porous and partially ordered structure of CNS-800. (d) ADF TEM micrograph and EELS thickness profile (inset) of CNS-800.

Scheme 1. Schematic of the synthesis process for the hemp-derived carbon nanosheets, with the three different structural layers S1, S2, and S3

more than 85% of the total wall thickness, is itself a layered structure consisting of microfibrils that are 10−30 nm in diameter.[33,35] Moreover these microfibrils consist of bundles of highly crystalline cellulose elementary fibrils (~2 nm in diameter) surrounded by semicellulose. Under the relatively aggressive hydrothermal conditions at 180 °C, most of semicellulose and part of lignin are converted into soluble organic compounds, while the crystalline cellulose is partially carbonized. Hence the S1 and S3 layers are removed, while the connections between the 10−30 nm diameter microfibrils in the S2 layer are loosened. In the subsequent activation process at 700−800 °C, the KOH melt penetrates into the loose connection between the microfibers, causing full separation of layers as sheets. Meanwhile, the layers are carbonized and activated by the KOH, further reducing their thickness and generating micro and mesoporosity.

It is worth pointing out that what is highlighted in Scheme 1 is a simplified schematic description of the process. The reactions occurring during hydrothermal carbonization of biomass are in fact quite complicated, involving hydrolysis, dehydration, decomposition, and condensation. The hydrothermal process can hydrolyze lignin and hemicellulose, decrease the crystallinity of cellulose, and increase the porosity of the biomass.[36] The high levels of oxygen-containing functional groups in the product of the hydrothermal synthesis process (defined as "biochar") make it highly reactive for subsequent chemical activation.[27] Supplementary Table S1 provides the carbon, oxygen, and nitrogen content as obtained from X-ray photoelectron spectroscopy (XPS), for the post hydrothermal hemp biochar, and the CNS

TABLE 1. Physical Parameters for Hemp-Derived Carbon Nanosheets and for Baseline Commercial Activated Carbon and Commercial Graphene Nanoplatelets

samples	S_{BET} (m^2 g^{-1})^a	S_{DFT} (m^2 g^{-1})^b	V_t (cm^3 g^{-1})^c	S_{micro} (m^2 g^{-1})^d	pore vol in cm^3 g^{-1e} and (pore vol %)			conductivity (S m^{-1})	I_G/I_D (L_a (nm))^g
					$V_{<1\ nm}$	$V_{1-2\ nm}$	$V_{>2\ nm}$		
CNS-700	1690	1340	1.08	1150	0.20 (22.5)	0.33 (37.1)	0.36 (40.4)	217	0.89 (3.92)
CNS-750	2287	1700	1.45	1375	0.23 (19.0)	0.45 (37.2)	0.53 (43.8)	211	0.85 (3.74)
CNS-800	1505	1160	1.26	880	0.16 (16.3)	0.25 (25.5)	0.57 (58.2)	226	0.93 (4.09)
AC	2050	1570	1.17	1323	0.23 (22.5)	0.40 (39.2)	0.39 (38.3)	$\sim$33^f	0.52 (2.29)
CG	726	637	1.37	439	0.085 (8.5)	0.095 (9.5)	0.82 (82.0)	294	1.55 (6.82)

^{a} Surface area was calculated with Brunauer—Emmett—Teller (BET) method, with a utilized pressure range from 0.05 to 0.20. ^{b} Surface area was calculated with density functional theory (DFT) method. ^{c} The total pore volume was determined at a relative pressure of 0.98. ^{d} The surface area of micropores was obtained by DFT analysis. ^{e} The volume of pores smaller than 1 nm ($V_{<1\ nm}$), pores between 1 and 2 nm ($V_{1-2\ nm}$), and pores larger than 2 nm ($V_{>2\ nm}$) was obtained by DFT analysis. ^{f} This value was obtained from the literature for activated carbon (Norit).[41] ^{g} L_a (= 4.4I_G/I_D (nm)) is the size of the graphitic domains.[39]

samples. The biochar has very high oxygen content and therefore should be responsive to the KOH treatment. As a comparison, we directly carbonized the hemp followed by KOH activation under the same conditions as CNS. The traditionally carbonized hemp bast fiber (pre-activation) shows a smooth surface and a dense structure (Supplementary Figure S5a). After activation (Supplementary Figure S5b), no layered structures were observed, further indicating the importance of hydrothermal process.

It is known that KOH activation will generate micro/mesopores inside carbons, with the surface area and porosity being controlled by the activation temperature.[18] Table 1 and Figure 2 provide details of the textural characteristics of the carbon materials. It can be seen that the surface area first increases with activation temperature, going from 1690 m^2 g^{-1} for CNS-700 to 2287 m^2 g^{-1} for CNS-750, and then decreases to 1505 m^2 g^{-1} for CNS-800. As Figure 2a demonstrated, type I/IV isotherms could be found for all samples. However the broadening of the knee in the relatively low-pressure range for CNS-750 and CNS-800 suggests small mesopores developing at increased activation temperatures. The amount of mesopores progressively increases with activation temperature. From Figure 2b, it is indicated that CNS-750 has the highest pore volume between 2 and 3 nm. On the other hand, mesopores larger than 3 nm are well developed for CNS-800 as a result of the widening of pre-existing pores.

Raman spectroscopy analysis was employed to further investigate the structure of the CNS specimens. The results are shown in Figure 2c and Supplementary Figure S6. All samples exhibit a broad disorder-induced D-band ($\sim$1330 cm^{-1}) and in-plane vibrational G-band ($\sim$1590 cm^{-1}).[37] In all of the carbon nanosheets the intensity of the G band is significantly higher than that of the D band, indicating that the nanosheets are partially graphitized. Moreover the ratio of the integrated intensities (I_G/I_D= 0.89 (CNS-700), 0.85 (CNS-750), and 0.93 (CNS-800)) is significantly higher than for the commercial

activated carbon (Norit, I_G/I_D= 0.52 (AC)). It is known that KOH activation tends to attack the aligned (i.e., graphitic) structural domains in a carbon matrix, resulting in a highly porous but disordered structure with relatively poor electrical conductivity.[38] However, the KOH-activated CNS samples show a relatively high degree of graphitization, which is related to the intrinsic complex hierarchical structure of the hemp precursor. As discussed earlier, hemp bast fiber contains a high content of crystalline cellulose. During the high temperature KOH activation, carbonization leads to structural alignment, while the breakdown of aligned structural domains occurs due to the intercalation of potassium compounds. The ultimate degree of graphitic order in the final product results from a balance of these competing processes. The lowest relative I_G/I_D ratio is at the intermediate activation temperature, supporting the argument regarding the competition between carbonization-induced ordering and activation-induced dissolution. Table 1 shows the calculated mean width (L_a) of the graphitic domains in each specimen, which is proportional to the I_G/I_D ratio.[39] The higher value of L_a indicates higher electrical conductivity can be expected.[40] The electrical conductivity of CNS samples, measured by the four-point probing method on a pellet compacted at 20 MPa die pressure, is 217, 211, 226 S m^{-1} for CNS-700, CNS-750, and CNS-800, respectively (Table 1). These values are much higher than what is reported for commercially available Norit activated carbon (33 S m^{-1} was obtained from literature,[41] since AC granules could not be compressed into pellets structurally stable enough for measurements) and are closer to what we obtained for commercial graphene nanoplatelets (Cheap Tubes Inc., labeled as CG, 294 S m^{-1}) measured identically. It is known that a partially graphitic carbon structure and a high level of interconnectedness ensures improved electrical conductivity in carbon-based electrodes,[42] which makes the CNS materials ideal for high power applications.

Supplementary Figure S7 presents the X-ray diffraction (XRD) patterns of the carbon nanosheets. There is a
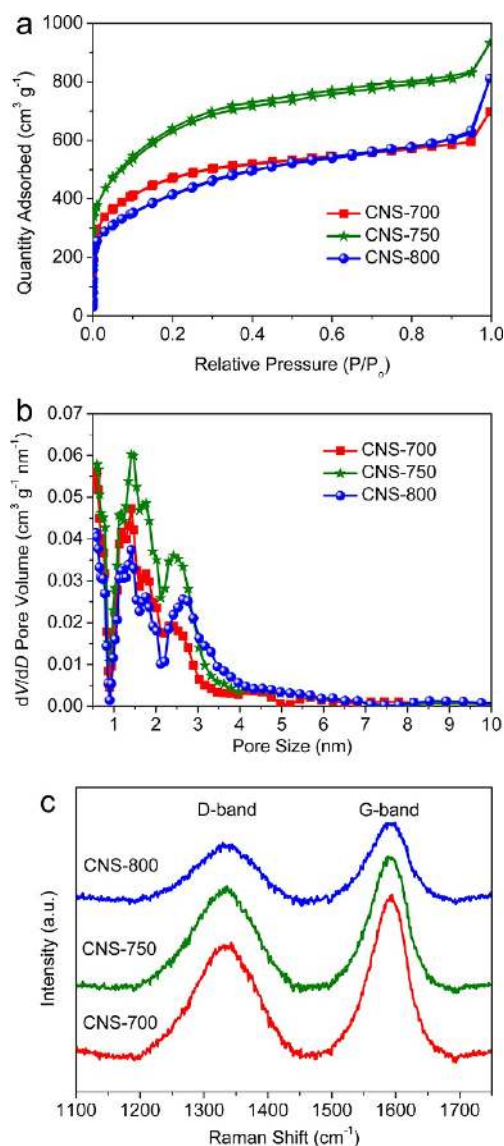
Figure 2. (a) Nitrogen adsorption−desorption isotherms of hemp-derived carbon nanosheets. **(b)** Pore size distribution calculated from the adsorption isotherms using DFT method. **(c)** Raman spectra of the resultant carbon nanosheets.

broad peak centered at $2\theta = 23°$, which corresponds to the (002) reflection of graphite. This value yields a basal plane interlayer distance of 0.39−0.40 nm. Based on the well-known Scherer equation, the c-axis length in the graphitic lattice can be estimated to be 1.4−1.5 nm. Therefore, the carbon nanosheets are composed of 3−4 layer-stacked graphene sheets (e.g., 1.5/0.39 = 3.84) surrounded by regions of disorder.

The partially graphitic and interconnected structure of the hemp-derived carbon nanosheets with developed hierarchical porosity is expected to yield exceptional electrochemical capacitive properties in an ionic liquid electrolyte (1-butyl-1-methylpyrrolidinium bis-(trifluoromethylsulfony)imide (BMPY TFSI, > 99%, Ionic Liquids Technologies Inc. USA)). Cyclic voltammetry (CV) was utilized to evaluate the electrochemical

performance of the CNS electrodes. Commercial activated carbon and commercial graphene nanoplatelets were also electrochemically tested as baselines. (The SEM, Raman, XPS, XRD and porosity analysis of baseline commercial AC and CG are displayed in Table 1 and Supplementary Table S1 and Figure S8.) Figure 3a shows the CV data for CNS-800 tested at 20 °C. Even at a high scan rate of 500 mV s^{-1}, the curve still maintains a quasi-rectangular shape, demonstrating excellent ion transport behavior even in a viscous ionic liquid. Supplementary Figure S9a compares the CV curves of CNS-700, CNS-750, CNS-800, commercial activated carbon, and commercial graphene nanoplatelets, all measured at 20 °C and 500 mV s^{-1}. The CNS samples (especially CNS-800) display significantly less distorted CV curves. The lack of distortion of the CNS CV curves compares quite favorably to published CVs of some state-of-the-art predominantly microporous carbons in ionic liquid electrolytes, tested at significantly lower rates (such as 100 mV s^{-1}) and at higher temperatures (such as 60 °C).[43,44] Supplementary Figure S9b shows the CV curves of CNS-800 tested at 0, 20, 60, and 100 °C, using the high scan rate of 500 mV s^{-1}. While the 0 °C CV curve is distorted due to the ion transport losses, the fact that any capacitance can be achieved at 0 °C and 500 mV s^{-1} is noteworthy (melting point of BMPY TFSI is −18 °C). Supplementary Figure S9c shows the CV curves of CNS-800 at scan rates from 100 to 500 mV s^{-1}, tested at 0 °C. The results demonstrate that at intermediate scan rates, such as 100 mV s^{-1}, a good capacitive response can be achieved even at such a low temperature. Overall such superior high rate-low temperature performance is comparable to some of the best performing graphene-based electrode materials[15,25] and has not been achieved *via* bioderived activated carbons. Supplementary Figure S9d and e shows the CV data for 60 and 100 °C. The ionic liquid displays higher ionic conductivity and lower viscosity at or above 60 °C, resulting in enhanced electric double-layer capacitance and decreased resistance for ion transport.

The galvanostatic charge−discharge profiles of CNS-800 tested at 0−100 °C are shown in Figure 3b. The curves are highly linear and symmetrical, meaning that the CNS electrodes have excellent electrochemical reversibility and Coulombic efficiency. For CNS-800, at a current density of 10 A g^{-1}, the IR drop is 0.08 V at 100 °C, 0.12 V at 60 °C, 0.23 V at 20 °C, and 0.57 V at 0 °C. While for all samples the IR drop increases with decreasing testing temperature, it does so the least for CNS-800. For example, at a scan rate of 10 A g^{-1} and tested at 20 °C (Supplementary Figure S10b), CNS-800 shows the smallest IR drop (0.23 V), followed by CNS-750 (0.25 V), CNS-700 (0.39 V), CG (0.51 V), and finally AC (0.56 V). It is generally accepted that the IR drop is related to the electrical conductivity and porous texture (including the tortuosity, connectivity, size distribution, and shape of pores) of the electrode.[32]
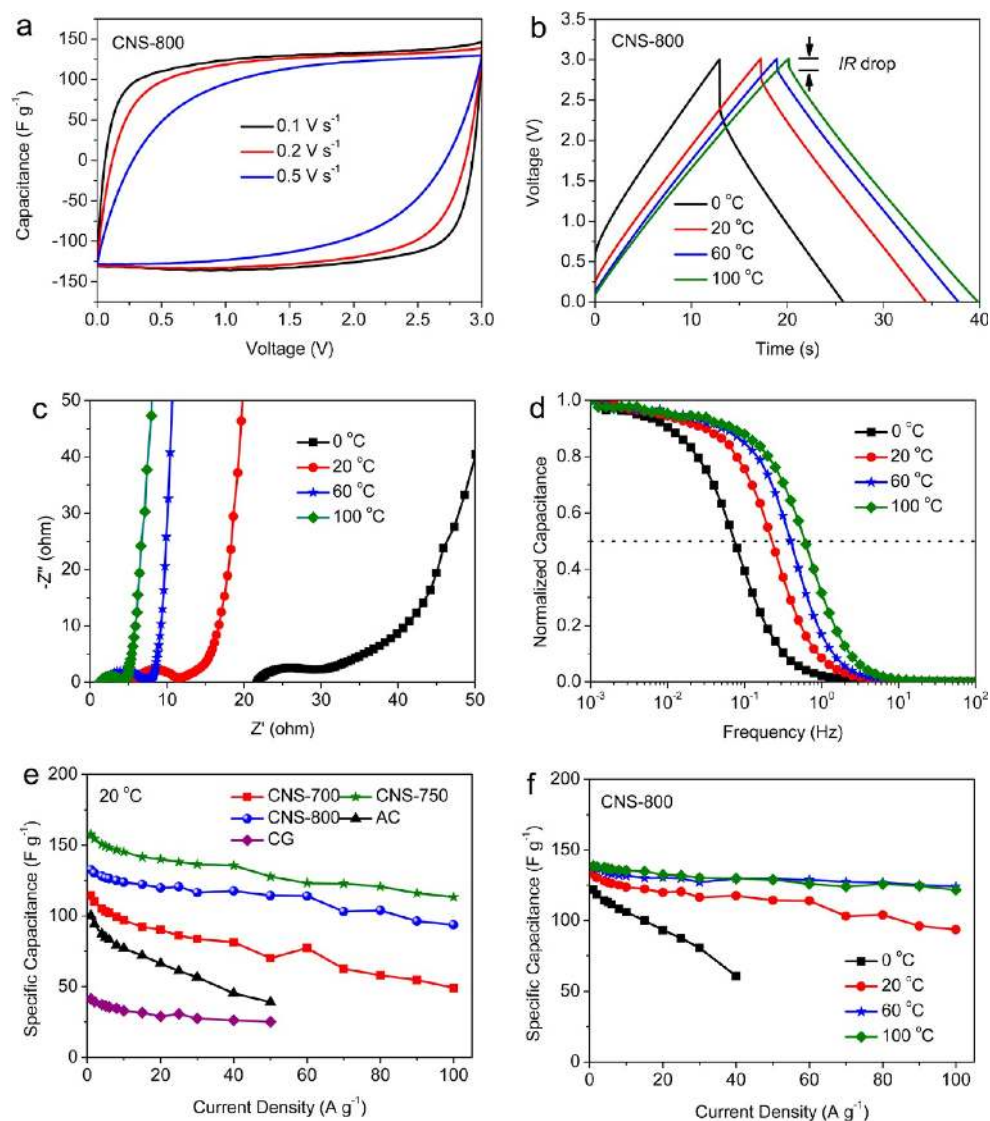
Figure 3. (a) CV curves of CNS-800 for three different scan rates, tested at 20 °C. (b) Galvanostatic charge−discharge profiles of CNS-800, at a current density of 10 A g^{-1}. (c) Nyquist plots and (d) frequency responses of CNS-800, measured at 0, 20, 60, and 100 °C. (e) Specific capacitance *versus* current density, tested at 20 °C, for the carbon nanosheets, baseline commercial activated carbon and baseline graphene nanoplatelets. (f) Specific capacitance *versus* current density for CNS-800 measured at different temperatures.

Specimen AC has the largest IR drop due to a combination the lowest electrode conductivity and the least optimum porous structure. The variation of the electrical conductivity and domain size between samples CNS-700, CNS-75,0 and CNS-800 is not significant, and we believe that CNS-700 with relative higher IR drop can be attributed to its lower percentage of volume of mesopores (40.4%) compared to that of CNS-750 (43.8%) and CNS-800 (58.2%). The BMPY TFSI electrolyte is high viscosous and contains ions of large diameters (the maximum dimension of the cation and the anion are 1.1 and 0.79 nm, respectively.[12,45]). The lack of a smooth inner-pore transport pathway will inevitably result in a significant ionic diffusional loss contribution to the IR drop. The lower graphitic character and the additional interfacial contact resistance

associated with packing of isolated micrometer-scale AC particles may result in higher resistance than the interconnected sheets of CNS. This is supported by Supplementary Figure S11, which is a Nyquist plot that demonstrates that the equivalent series resistances of the CNS samples are all on par ($\sim$ 6 Ω), while that of the AC is substantially higher ($\sim$30 Ω).

Electrochemical impedance spectroscopy further confirms the favorable performance of the carbon nanosheets. Figure 3c shows the Nyquist plots of CNS-800, measured at 0, 20, 60, and 100 °C. The real axis intercept represents the equivalent series resistance, which is a combination of ionic resistance of the electrolyte, electrical resistance of the electrode, and contact resistance at the active material/current collector interface.[18] The increase in the equivalent series

resistance with decreasing temperature may largely be attributed to the changes in the ionic resistance of the electrolyte, since the electrical resistance of the electrode and the contact resistance would not vary substantially over the 100 °C window. The projected length of the Warburg-type line (the 45° segment) is related to the ion diffusion limitations within the electrode material.[46] The diffusion of electrolyte ions stopped at about 0.5, 2, 6.3, and 15.8 Hz at 0, 20, 60, and 100 °C, respectively, showing improved frequency response with increased testing temperature. Such frequency response is comparable to that of a recently reported activated graphene.[15] Bode plots of the frequency response of capacitance are presented in Figure 3d. The operating frequency at which the capacitance is 50% of its maximum value increased from 0.075 (0 °C) to 0.22 (20 °C), 0.39 (60 °C), and 0.62 Hz (100 °C). These values of operating frequency are quite high for supercapacitors employing ionic liquid electrolytes. They are comparable to what was obtained for state-of-the-art ordered mesoporous carbide derived carbons (0.1−0.7 Hz in an ionic liquid) and higher than what was previously reported for optimized activated hydrothermal carbons (0.1 Hz in organic electrolyte) and advanced polypyrrole-derived activated carbons (∼0.06 Hz in ionic liquid electrolyte at 60 °C).[17,18,47]

Figure 3e and f and Supplementary Figure S12 show the specific capacitance *versus* current density, tested at 0−100 °C, for the carbon nanosheets, commercial activated carbon, and graphene nanoplatelets. At 20−100 °C, CNS-750 exhibits the largest capacitance due to its overall highest accessible surface area. At 0 °C, CNS-800 has better performance at scan rates higher than 5 A g^{-1}, while CNS-750 is superior at the lower scan rates. The performance transition from CNS-750 to CNS-800 at 0 °C is mainly attributed to the role of the pore size and shape in determining the ion adsorption characteristics. At 0 °C and higher currents, the micropores could give rise to higher ohmic resistance due to the ion "traffic jam",[17] leading to the decrease of capacitance from micropores. In this case, the net capacitance is in part dictated by the surface area associated with mesoporosity. Interestingly, we noted that the better performed sample (CNS-800) has lower specific surface area from mesopores (280 m² g^{-1}) than CNS-750 (325 m² g^{-1}). This seemingly contradictory result might be attributed to the effect of pore/surface curvature. It is intuitive that highly curved and tortuous inner pore surfaces would lead to more diffusional losses and less effective ion adsorption as compared to more planar ones. Although it is difficult to determine the exact pore shape of these samples, we noted that the average mesopore size of CNS-800 (4.3 nm) is larger than that of CNS-750 (3.4 nm) judging from the pore size distributions (Figure 2b). It has been recently demonstrated that the surface area

normalized capacitance increased with increasing pore size in the 2−5 nm pore range,[48,49] and therefore CNS-800 should have higher surface area normalized capacitance from mesopores. In general, CNS-800s mesoporosity combined with the short diffusion distances normal to the nanosheet thickness allows for facile ion transport and provides high capacitance at low temperature and high rates.

At 20 °C and 100 A g^{-1}, both CNS-750 and CNS-800 retain more than 70% of their capacitance at 1 A g^{-1}. This amazing capacitance retention is ascribed to the high mesopore volume and nanoscale diffusion pathway that allows for rapid ion transport. The capacity retention ratio for carbon nanosheets at 100 A g^{-1} is as high as 72−92% when measured at 60 and 100 °C. Even tested at 0 °C, the capacitance of CNS-800 can reach 122 F g^{-1} at 1 A g^{-1}, with 66% of the capacitance still being delivered at 30 A g^{-1}. At 20 °C and 1 A g^{-1} the surface area normalized capacitance for CNS-700, CNS-750, and CNS-800 was, respectively, 6.8, 6.9, and 8.8 μF cm^{-2} (based on BET surface area) and 8.5, 9.3, and 11.4 μF cm^{-2} (based on DFT surface area). These values are much higher than those of commercial activated carbon (4.9/6.4 μF cm^{-2}, BET/DFT) and graphene nanoplatelets (5.7/6.5 μF cm^{-2} BET/DFT). Overall, CNS-800 achieved the highest surface area normalized capacitance, which is higher than recently reported activated graphene (6.9 μF cm^{-2}) and close to polypyrrole-derived activated carbon and carbide-derived carbons (7−14 μF cm^{-2}).[12,15,18]

Figure 4a shows the Ragone plot of CNS-800 at different testing temperatures, with the specific energy and power being based on the mass of the active materials in a two-electrode configuration. Supplementary Figure S13 shows similar active mass normalized Ragone plots comparing CNS-700, CNS-750, CNS-800, commercial activated carbon, and graphene nanoplatelets, evaluated at 0−100 °C. When tested at 20 °C, CNS-750 and CNS-800 exhibit high energy density of about 19 and 18 Wh kg^{-1} at a power of 20 kW kg^{-1}. This energy density is increased to 34/31 and 40/34 Wh kg^{-1} at 60 and 100 °C, respectively. Even testing at room temperature, CNS samples can still exceed the PNGV power target (15 kW kg^{-1}, in terms of electrode active material) with high energy density.[32] In the temperature range of 0−100 °C, CNS samples have much better energy−power characteristics than AC and CG. The exceptional energy characteristic of the CNS specimens is fully expected given their high specific capacitance at most scan rates/temperatures (see Methods section for detailed calculations). We also compare the energy density and power density of the CNS electrode to those of other reported activated carbon, mesoprous carbon, carbon nanotube, and graphene electrodes based on electrode active mass (Figure 4b).[7,9,11,14,22,25,43,50−54] Comparatively the CNS electrodes exhibit comparable or even higher energy
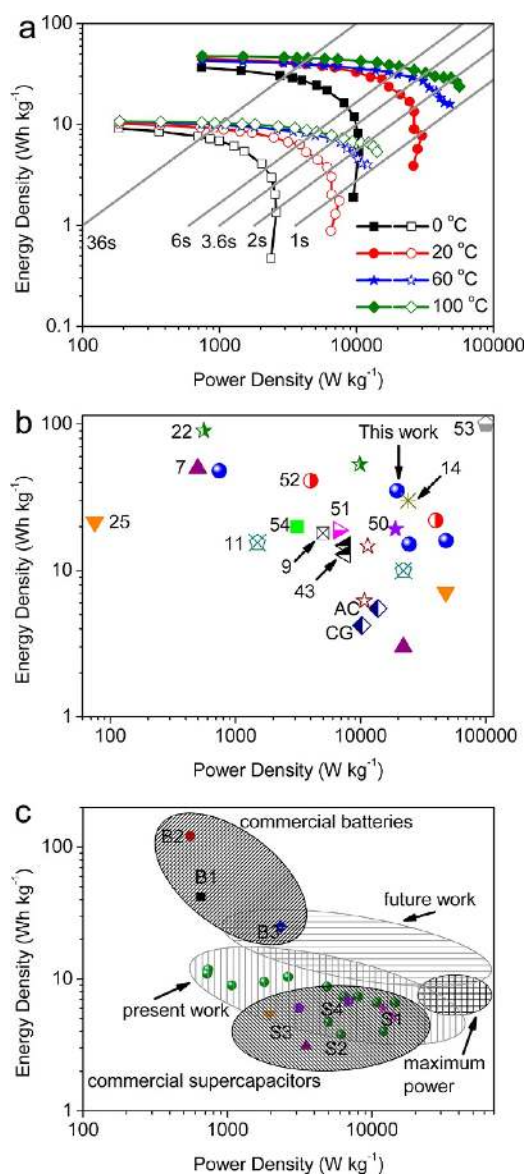
Figure 4. (a) Ragone chart of CNS-800 evaluated at different temperatures. The energy and power density were normalized to the total mass of device (hollow) and the mass of active material (solid). (b) Performance comparison (on an active mass normalized basis) of hemp-derived carbon nanosheets *versus* literature reported values for state-of-the-art mesoporous carbons, activated carbons, carbon nanotubes, and graphene tested at 20−60 °C. (c) Performance comparison of CNS-based device measured at 20−100 °C for commercial batteries and supercapacitors (Data from refs 57 and 58. B1: Panasonic NiHD. B2: Sanyo Li-ion. B3: Bolder Pd-acid. S1: Maxwell BCAP3000 and BCAP0310. S2: Panasonic 800F. S3: Superfarad 250 F. S4: Saft Gen2 and Gen3.). The values for commercial batteries and supercapacitors are the maximum energy and power densities.

densities and substantially higher power densities. When considering all components of the packaged cell, the carbon weight accounts for about 30% of the total mass of the packaged device.[15,55,56] A factor of 4 was used to extrapolate the energy−power density of the cell from the performance based on active material. Figure 4a also shows the Ragone plot of CNS-800 at different testing

temperatures, with the specific energy and power being based on the total device mass. Figure 4c compares the performance of CNS-based devices with commercial batteries and supercapacitors. The values for commercial batteries and supercapacitors are the maximum energy and power densities reported.[57,58] The estimated maximum energy density of our device obtained at an operating voltage of 3.0 V is ∼12 Wh kg^{-1}, which is higher than that of commercially available supercapacitors. An energy density of 8−10 Wh kg^{-1} can be achieved for CNS-based device, and the device can be completely recharged in less than 6 s. Based on the cell internal resistance values determined from the IR loss values,[59] the maximum power density of CNS-800 tested at 20 °C is 28 kW kg^{-1} based on total device, and this value increased to 49 kW kg^{-1} at 60 °C and 77 kW kg^{-1} at 100 °C, which is about 10−100 times higher than commercial batteries. From Figure 4c, we may argue that when an ionic liquid with a wider electrochemical window (such as ∼4 V) was employed, the CNS-based devices may actually bridge the energy gap between commercial batteries and supercapacitors.

Electrochemical cycling stability of CNS-800, tested at 10 A g^{-1}, is shown in Supplementary Figure S14. The specific capacitance decreases slightly (8%) after the initial 1000 cycles. However then the capacitance increases and remains at 96% of the initial capacitance even after 10,000 cycles. The cycling-induced improvement observed after 1000 cycles may be attributed to improved pore wetting by the ionic liquid electrolyte or perhaps to *in situ* activation of the electrode to expose additional surface area.

To summarize, the unparalleled high rate capability, low temperature performance, high frequency response, and long cycle life of our obtained carbon nanosheet materials can be ascribed to several microstructural (pore structure and carbon structure) factors: The carbons are highly interconnected and partially graphitic, yielding excellent electrically conductive electrode. The macroporous voids with diameters of 1−2 μm serve as ion-buffering reservoirs. The low thickness of the carbon nanosheets (10−30 nm) ensures nanoscale distances (5−15 nm) for ion diffusion. The high total content of mesopores facilitates the accessibility of the electrolyte ions to the electrode surface and allows for fast ion transport.

CONCLUSION

Here we report the successful hydrothermal-based synthesis of two-dimensional, yet interconnected, carbon nanosheets with superior electrochemical storage properties comparable to those of state-of-the-art graphene-based electrodes. We were able to achieve this by employing a biomass precursor with a unique structure, hemp bast fiber. The resultant graphene-like nanosheets possess fundamentally different properties (pore size distribution, physical interconnectedness,

and electrical conductivity) as compared to conventional biomass-derived activated carbons. The electrodes fabricated from our materials work down to 0 °C and display some of the best power−energy combinations reported in the literature for any carbon. For example, at a very high power density of 20 kW kg^{-1} and 20, 60, and 100 °C, the energy densities are 19, 34, and 40 Wh kg^{-1}, respectively. When the entire device is considered, an energy density of 8−10 Wh kg^{-1} can be achieved at a charge time less than 6 s.

METHODS

Material Preparation. Carbon nanosheets were prepared by carbonization and activation of the hydrothermal product of hemp bast fiber (volatile content, 81.98 wt %; ash content, 2.95 wt %). Detailed procedures are as follows: 3.0 g of hemp bast fiber and 50 mL of diluted sulfuric acid were placed in a 120-mL stainless steel autoclave. The autoclave was sealed and heated at 180 °C for 24 h and then allowed to cool to room temperature. The resulting carbonaceous solid, denoted as biochar, was recovered by filtration, washed with distilled water, and dried. The biochar material was chemically activated using potassium hydroxide. The biochar and KOH were thoroughly ground in an agate mortar in a 1:1 mass ratio, and then the mixture was heated at 700−800 °C (3 °C min^{-1}) for 1 h under argon flow. After that, the activated samples were thoroughly washed with 10 wt % HCl and distilled water. Finally, the carbons were dried in an oven at 100 °C for 12 h.

Material Characterization. SEM was conducted with a Hitachi-4800 scanning electron microscope. TEM was performed using the JEOL 2010 microscope at 200 kV. XRD analysis was performed using a Bruker AXS D8 Discover diffractometer with a Cu Kα radiation source. XPS is obtained on an Axis Ultra spectrometer. Raman spectroscopy analysis was performed with a confocal microprobe Raman system (Thermo Nicolet Almega XR Raman Microscope). Nitrogen adsorption−desorption analysis was performed using Quantachrome Instruments (U.S.A) Autosorb-1 at −196 °C. The conductivity is measured by Pro4 from Lucas Laboratories.

Electrochemical Measurement. A slurry of 80 wt % carbon material, 10 wt % carbon black, and 10 wt % poly(vinylidenedifluoride) in N-methyl pyrrolidone was coated onto a stainless steel disc (∼2 mg cm^{-2}, 50−100 μm thick) and then dried at 100 °C overnight in vacuum oven. A total of 2032 stainless steel coin cells with two symmetrical carbon electrodes separated by a porous polymetric separator were assembled inside an Ar-filled glovebox (<0.1 ppm of both oxygen and H$_2$O). Cyclic voltammetry curves, galvanostatic charge−discharge profiles, and electrochemical impedance spectroscopy measurements were measured using a Solartron 1470E Multichannel Potentiostat/Cell Test System. The gravimetric capacitance for a single electrode, C_g (F g^{-1}), was calculated on the basis of charge−discharge profiles according to

$$C_g = \frac{2I}{(dV/dt)m}$$

where I is the current (A), dV/dt is the slope of the discharge curve after the ohmic drop (V s^{-1}), and m is the mass (g) of active material in each electrode. The energy density (E, Wh kg^{-1}) and power density (P, W kg^{-1}) (on an active mass normalized basis) were calculated according to

$$E = \frac{1}{2}C_g V^2 \cdot \frac{1}{4} \cdot \frac{1}{3.6}$$

$$P = \frac{E}{t}$$

where V is the cell voltage after ohmic drop (V) and t is the discharge time (h). The maximum power density (P_{max}, kW kg^{-1}) was calculated based on the internal resistance (R_s) of the cell, which can be obtained by fitting the relationship between IR drop and current density. Linear fit model for IR drop is IR$_{drop}$ = $a + bI$, where a represents the difference between the 3 V applied and the charged potential of the supercapacitor, b represents double the value of R_s, and I is the discharge current.[59]

$$P_{max} = \frac{V_{OCV}^2}{4R_s} = \frac{(3-a)^2}{2b}$$

REFERENCES AND NOTES

1. Conway, B. E. *Electrochemical Supercapacitors: Scientific Fundamentals and Technological Applications*; Kluwer Academic/Plenum: New York, 1999.
2. Simon, P.; Gogotsi, Y. Materials for Electrochemical Capacitors. *Nat. Mater.* **2008**, *7*, 845–854.
3. Lin, R. Y.; Taberna, P. L.; Fantini, S.; Presser, V.; Pérez, C. R.; Malbosc, F.; Rupesinghe, N. L.; Teo, K. B. K.; Gogotsi, Y.; Simon, P. Capacitive Energy Storage from −50 to 100 °C Using an Ionic Liquid Electrolyte. *J. Phys. Chem. Lett.* **2011**, *2*, 2396–2401.
4. Armand, M.; Endres, F.; MacFarlane, D. R.; Ohno, H.; Scrosati, B. Ionic-Liquid Materials for the Electrochemical Challenges of the Future. *Nat. Mater.* **2009**, *8*, 621–629.
5. Arbizzani, C.; Biso, M.; Cericola, D.; Lazzari, M.; Soavi, F.; Mastragostino, M. Safe, High-Energy Supercapacitors Based on Solvent-Free Ionic Liquid Electrolytes. *J. Power Sources* **2008**, *185*, 1575–1579.
6. Frackowiak, E.; Béguin, F. Carbon Materials for the Electrochemical Storage of Energy in Capacitors. *Carbon* **2001**, *39*, 937–950.
7. Lu, W.; Hartman, R.; Qu, L. T.; Dai, L. M. Nanocomposite Electrodes for High-Performance Supercapacitors. *J. Phys. Chem. Lett.* **2011**, *2*, 655–660.
8. Balducci, A.; Dugas, R.; Taberna, P. L.; Simon, P.; Plée, D.; Mastragostino, M.; Passerini, S. High Temperature Carbon-Carbon Supercapacitor Using Ionic Liquid as Electrolyte. *J. Power Sources* **2007**, *165*, 922–927.
9. Lazzari, M.; Soavi, F.; Mastragostino, M. Mesoporous Carbon Design for Ionic Liquid-Based, Double-Layer Supercapacitors. *Fuel Cells* **2010**, *10*, 840–847.
10. Xu, B.; Wu, F.; Chen, R. J.; Cao, G. P.; Chen, S.; Yang, Y. S. Mesoporous Activated Carbon Fiber as Electrode Material for High-Performance Electrochemical Double Layer Capacitors with Ionic Liquid Electrolyte. *J. Power Sources* **2010**, *195*, 2118–2124.
11. Kang, Y. J.; Chun, S. J.; Lee, S. S.; Kim, B. Y.; Kim, J. H.; Chung, H.; Lee, S. Y.; Kim, W. All-Solid-State Flexible Supercapacitors Fabricated with Bacterial Nanocellulose Papers, Carbon Nanotubes, and Triblock-Copolymer Ion Gels. *ACS Nano* **2012**, *6*, 6400–6406.
12. Largeot, C.; Portet, C.; Chmiola, J.; Taberna, P. L.; Gogotsi, Y.; Simon, P. Relation between the Ion Size and Pore Size for an Electric Double-Layer Capacitor. *J. Am. Chem. Soc.* **2008**, *130*, 2730–2731.
13. Stoller, M. D.; Park, S. J.; Zhu, Y. W.; An, J. H.; Ruoff, R. S. Graphene-Based Ultracapacitors. *Nano Lett.* **2008**, *8*, 3498–3502.

14. Kim, T. Y.; Lee, H. W.; Stoller, M.; Dreyer, D. R.; Bielawski, C. W.; Ruoff, R. S.; Suh, K. S. High-Performance Supercapacitors Based on Poly(ionic liquid)-Modified Graphene Electrodes. *ACS Nano* **2011**, *5*, 436–442.

15. Zhu, Y. W.; Murali, S.; Stoller, M. D.; Ganesh, K. J.; Cai, W. W.; Ferreira, P. J.; Pirkle, A.; Wallace, R. M.; Cychosz, K. A.; Thommes, M.; et al. Carbon-Based Supercapacitors Produced by Activation of Graphene. *Science* **2011**, *332*, 1537–1541.

16. Wei, L.; Yushin, G. Nanostructured Activated Carbons from Natural Precursors for Electrical Double Layer Capacitors. *Nano Energy* **2012**, *1*, 552–565.

17. Wei, L.; Sevilla, M.; Fuertes, A. B.; Mokaya, R.; Yushin, G. Hydrothermal Carbonization of Abundant Renewable Natural Organic Chemicals for High-Performance Supercapacitor Electrodes. *Adv. Energy Mater.* **2011**, *1*, 356–361.

18. Wei, L.; Sevilla, M.; Fuertes, A. B.; Mokaya, R.; Yushin, G. Polypyrrole-Derived Activated Carbons for High-Performance Electrical Double-Layer Capacitors with Ionic Liquid Electrolyte. *Adv. Funct. Mater.* **2012**, *22*, 827–834.

19. Wang, D. W.; Li, F.; Liu, M.; Lu, G. Q.; Cheng, H. M. Mesopore-Aspect-Ratio Dependence of Ion Transport in Rodtype Ordered Mesoporous Carbon. *J. Phys. Chem. C* **2008**, *112*, 9950–9955.

20. Fan, Z. J.; Liu, Y.; Yan, J.; Ning, G. Q.; Wang, Q.; Wei, T.; Zhi, L. J.; Wei, F. Template-Directed Synthesis of Pillared-Porous Carbon Nanosheet Architectures: High-Performance Electrode Materials for Supercapacitors. *Adv. Energy Mater.* **2012**, *2*, 419–424.

21. Huang, Z. D.; Zhang, B. A.; Oh, S. W.; Zheng, Q. B.; Lin, X. Y.; Yousefi, N.; Kim, J. K. Self-Assembled Reduced Graphene Oxide/Carbon Nanotube Thin Films as Electrodes for Supercapacitors. *J. Mater. Chem.* **2012**, *22*, 3591–3599.

22. Liu, C. G.; Yu, Z. N.; Neff, D.; Zhamu, A.; Jang, B. Z. Graphene-Based Supercapacitor with an Ultrahigh Energy Density. *Nano Lett.* **2010**, *10*, 4863–4868.

23. El-Kady, M. F.; Strong, V.; Dubin, S.; Kaner, R. B. Laser Scribing of High-Performance and Flexible Graphene-Based Electrochemical Capacitors. *Science* **2012**, *335*, 1326–1330.

24. Yoo, J. J.; Balakrishnan, K.; Huang, J. S.; Meunier, V.; Sumpter, B. G.; Srivastava, A.; Conway, M.; Reddy, A. L. M.; Yu, J.; Vajtai, R.; et al. Ultrathin Planar Graphene Supercapacitors. *Nano Lett.* **2011**, *11*, 1423–1427.

25. Xu, Z. W.; Li, Z.; Holt, C. M. B.; Tan, X. H.; Wang, H. L.; Amirkhiz, B. S.; Stephenson, T.; Mitlin, D. Electrochemical Supercapacitor Electrodes from Sponge-Like Graphene Nanoarchitectures with Ultrahigh Power Density. *J. Phys. Chem. Lett.* **2012**, *3*, 2928–2933.

26. Chen, Z. P.; Ren, W. C.; Gao, L. B.; Liu, B. L.; Pei, S. F.; Cheng, H. M. Three-Dimensional Flexible and Conductive Interconnected Graphene Networks Grown by Chemical Vapour Deposition. *Nat. Mater.* **2011**, *10*, 424–428.

27. Sevilla, M.; Fuertes, A. B.; Mokaya, R. High Density Hydrogen Storage in Superactivated Carbons from Hydrothermally Carbonized Renewable Organic Materials. *Energy Environ. Sci.* **2011**, *4*, 1400–1410.

28. Cheng, F.; Liang, J.; Zhao, J.; Tao, Z.; Chen, J. Biomass Waste-Derived Microporous Carbons with Controlled Texture and Enhanced Hydrogen Uptake. *Chem. Mater.* **2008**, *20*, 1889–1895.

29. Rosas, J. M.; Bedia, J.; Rodriguez-Mirasol, J.; Cordero, T. Preparation of Hemp-Derived Activated Carbon Monoliths. Adsorption of Water Vapor. *Ind. Eng. Chem. Res.* **2008**, *47*, 1288–1296.

30. Rosas, J. M.; Bedia, J.; Rodriguez-Mirasol, J.; Cordero, T. HEMP-Derived Activated Carbon Fibers by Chemical Activation with Phosphoric Acid. *Fuel* **2009**, *88*, 19–26.

31. Yang, R.; Liu, G. Q.; Xu, X. H.; Li, M.; Zhang, J. C.; Hao, X. M. Surface Texture, Chemistry and Adsorption Properties of Acid Blue 9 of Hemp (Cannabis Sativa L.) Bast-Based Activated Carbon Fibers Prepared by Phosphoric Acid Activation. *Biomass Bioenergy* **2011**, *35*, 437–445.

32. Wang, D. W.; Li, F.; Liu, M.; Lu, G. Q.; Cheng, H. M. 3D Aperiodic Hierarchical Porous Graphitic Carbon Material for High-Rate Electrochemical Capacitive Energy Storage. *Angew. Chem., Int. Ed.* **2008**, *47*, 373–376.

33. Fan, M.; Dai, D.; Yang, A. High Strength Natural Fiber Composite: Defibrillation and its Mechanisms of Nano Cellulose Hemp Fibers. *Int. J. Polym. Mater.* **2011**, *60*, 1026–1040.

34. van den Broeck, H. C.; Maliepaard, C.; Ebskamp, M. J. M.; Toonen, M. A. J.; Koops, A. J. Differential Expression of Genes Involved in C-1 Metabolism and Lignin Biosynthesis in Wooden Core and Bast Tissues of Fibre Hemp (Cannabis Sativa L.). *Plant Sci.* **2008**, *174*, 205–220.

35. Thygesen, A.; Daniel, G.; Lilholt, H.; Thomsen, A. B. Hemp Fiber Microstructure and Use of Fungal Defibration to Obtain Fibers for Composite Materials. *J. Nat. Fibers* **2005**, *2*, 19–37.

36. Kumar, P.; Barrett, D. M.; Delwiche, M. J.; Stroeve, P. Methods for Pretreatment of Lignocellulosic Biomass for Efficient Hydrolysis and Biofuel Production. *Ind. Eng. Chem. Res.* **2009**, *48*, 3713–3729.

37. Portet, C.; Yushin, G.; Gogotsi, Y. Electrochemical Performance of Carbon Onions, Nanodiamonds, Carbon Black and Multiwalled Carbon Nanotubes in Electrical Double Layer Capacitors. *Carbon* **2007**, *45*, 2511–2518.

38. Subramanian, V.; Luo, C.; Stephan, A. M.; Nahm, K. S.; Thomas, S.; Wei, B. Q. Supercapacitors from Activated Carbon Derived from Banana Fibers. *J. Phys. Chem. C* **2007**, *111*, 7527–7531.

39. Knight, D. S.; White, W. B. Characterization of Diamond Films by Raman Spectroscopy. *J. Mater. Res.* **1989**, *4*, 385–393.

40. Cho, Y. D.; Fey, G. T. K.; Kao, H. M. The Effect of Carbon Coating Thickness on the Capacity of LiFePO$_4$/C composite Cathodes. *J. Power Sources* **2009**, *189*, 256–262.

41. Gamby, J.; Taberna, P. L.; Simon, P.; Fauvarque, J. F.; Chesneau, M. Studies and Characterisations of Various Activated Carbons Used for Carbon/Carbon Supercapacitors. *J. Power Sources* **2001**, *101*, 109–116.

42. Li, Z.; Zhang, L.; Amirkhiz, B. S.; Tan, X. H.; Xu, Z. W.; Wang, H. L.; Olsen, B. C.; Holt, C. M. B.; Mitlin, D. Carbonized Chicken Eggshell Membranes with 3D Architectures as High-Performance Electrode Materials for Supercapacitors. *Adv. Energy Mater.* **2012**, *2*, 431–437.

43. Zhou, J.; Yuan, X.; Xing, W.; Si, W. J.; Zhuo, S. P. Capacitive Performance of Mesoporous Carbons Derived from the Citrates in Ionic Liquid. *Carbon* **2010**, *48*, 2765–2772.

44. Wei, L.; Yushin, G. Electrical Double Layer Capacitors with Sucrose Derived Carbon Electrodes in Ionic Liquid Electrolytes. *J. Power Sources* **2011**, *196*, 4072–4079.

45. Largeot, C.; Taberna, P. L.; Gogotsi, Y.; Simon, P. Microporous Carbon-Based Electrical Double Layer Capacitor Operating at High Temperature in Ionic Liquid Electrolyte. *Electrochem. Solid-State Lett.* **2011**, *14*, A174–A176.

46. Yang, X. W.; Zhu, J. W.; Qiu, L.; Li, D. Bioinspired Effective Prevention of Restacking in Multilayered Graphene Films: Towards the Next Generation of High-Performance Supercapacitors. *Adv. Mater.* **2011**, *23*, 2833–2838.

47. Rose, M.; Korenblit, Y.; Kockrick, E.; Borchardt, L.; Oschatz, M.; Kaskel, S.; Yushin, G. Hierarchical Micro- and Mesoporous Carbide-Derived Carbon as a High-Performance Electrode Material in Supercapacitors. *Small* **2011**, *7*, 1108–1117.

48. Chmiola, J.; Yushin, G.; Gogotsi, Y.; Portet, C.; Simon, P.; Taberna, P. L. Anomalous Increase in Carbon Capacitance at Pore Sizes Less Than 1 Nanometer. *Science* **2006**, *313*, 1760–1763.

49. Huang, J.; Sumpter, B. G.; Meunier, V. A Universal Model for Nanoporous Carbon Supercapacitors Applicable to Diverse Pore Regimes, Carbon Materials, and Electrolytes. *Chem.—Eur. J.* **2008**, *14*, 6614–6626.

50. Krause, A.; Balducci, A. High Voltage Electrochemical Double Layer Capacitor Containing Mixtures of Ionic Liquids and Organic Carbonate as Electrolytes. *Electrochem. Commun.* **2011**, *13*, 814–817.

51. Pandey, G. P.; Hashmi, S. A.; Kumar, Y. Performance Studies of Activated Charcoal Based Electrical Double Layer Capacitors with Ionic Liquid Gel Polymer Electrolytes. *Energy Fuels* **2010**, *24*, 6644–6652.

52. Kang, Y. J.; Chung, H.; Han, C. H.; Kim, W. All-Solid-State Flexible Supercapacitors Based on Papers Coated with Carbon Nanotubes and Ionic-Liquid-Based Gel Electrolytes. *Nanotechnology* **2012**, *23*, 065401.

53. Lu, W.; Qu, L. T.; Henry, K.; Dai, L. M. High Performance Electrochemical Capacitors from Aligned Carbon Nanotube Electrodes and Ionic Liquid Electrolytes. *J. Power Sources* **2009**, *189*, 1270–1277.

54. Sun, G. H.; Li, K. X.; Xie, L. J.; Wang, J. L.; Li, Y. Q. Preparation of Mesoporous Carbon Spheres with a Bimodal Pore Size Distribution and Its Application for Electrochemical Double Layer Capacitors Based on Ionic Liquid as the Electrolyte. *Microporous Mesoporous Mater.* **2012**, *151*, 282–286.

55. Gogotsi, Y.; Simon, P. True Performance Metrics in Electrochemical Energy Storage. *Science* **2011**, *334*, 917–918.

56. Stoller, M. D.; Ruoff, R. S. Best Practice Methods for Determining an Electrode Material's Performance for Ultracapacitors. *Energy Environ. Sci.* **2010**, *3*, 1294–1301.

57. Burke, A. Ultracapacitors: Why, How, and Where is the Technology. *J. Power Sources* **2000**, *91*, 37–50.

58. Maxwell Technologies (www.maxwell.com), data based on their medium cell with highest power density available (model BCAP3000 and BCAP3010).

59. Izadi-Najafabadi, A.; Yamada, T.; Futaba, D. N.; Yudasaka, M.; Takagi, H.; Hatori, H.; Iijima, S.; Hata, K. High-Power Supercapacitor Electrodes from Single-Walled Carbon Nanohorn/Nanotube Composite. *ACS Nano* **2011**, *5*, 811–819.